

C. HENDRICH¹
L. FAVRE¹
D.N. IEVLEV¹
A.N. DOBRYNIN¹
W. BRAS²
U. HÖRMANN³
E. PISCOPIELLO³
G. VAN TENDELOO³
P. LIEVENS^{1,✉}
K. TEMST¹

Measurement of the size of embedded metal clusters by mass spectrometry, transmission electron microscopy, and small-angle X-ray scattering

¹ Laboratorium voor Vaste-Stoffysica en Magnetisme en INPAC – Institute for Nanoscale Physics and Chemistry, K.U.Leuven, Celestijnenlaan 200 D, 3001 Leuven, Belgium

² DUBBLE@ESRF, Netherlands Organisation for Scientific Research (NWO), 6 Rue Jules Horowitz, 38043 Grenoble, France

³ Elektronenmicroscopie voor Materiaalonderzoek, Universiteit Antwerpen, Groenenborgerlaan 171, 2020 Antwerp, Belgium

Received: 14 July 2006/Accepted: 21 November 2006
Published online: 12 January 2007 • © Springer-Verlag 2007

ABSTRACT Ensembles of nanometer-sized Au, Co, Er, and FePt clusters were generated by a laser vaporization source and embedded in a MgO matrix grown on a mica substrate. The size distribution of the clusters was measured before sample preparation by time-of-flight mass spectrometry and afterwards by transmission electron microscopy. These well-characterized samples were used for investigations by small-angle X-ray scattering (SAXS). The scattering data was evaluated by Guinier analysis providing the average radii of the embedded clusters. The results are in good agreement with the cluster sizes obtained from the mass spectra as well as the dimensions determined from the transmission electron micrographs. Furthermore, other samples which were produced at an elevated substrate temperature of 500 °C exhibited an increased average cluster radius in the SAXS measurements. This behavior is attributed to diffusion and coalescence emerging at higher deposition temperatures.

PACS 61.10.Eq; 61.46.+w; 68.37.Lp; 81.07.-b

1 Introduction

Nanometer-scale materials containing metal clusters show a number of unexpected properties [1–7]. These are due to quantum confinement effects, large surface-to-volume ratios, or to changed interatomic lattice distances of the clusters. The anomalies in the size-dependent catalytic activity [4], the melting point [5], the optical properties [6], and the magnetic properties [2, 7] can be mentioned as examples. Nanoparticles are interesting for their potential technological applications since they can be used as building blocks of larger devices [8] and there are applications for optoelectronic devices [9] and magnetic data storage [10].

The production of nanometer-sized materials is an elaborate procedure. The subsequent characterization of the nanoparticles is a complex but important task. In particular, the determination of the size of particles with dimensions below 3 nm is fairly complex. Scanning probe microscopy

(SPM) is only useful for exposed non-embedded particles and the particle shape is convoluted with that of the probe tip [11]. Transmission electron microscopy (TEM) often requires special sample preparation, e.g. ion-beam processing [12], which is a destructive method. This issue can be avoided by the use of TEM grids, but has as disadvantage that there is no choice of substrate material. Moreover, SPM and TEM are limited to small sections of the samples and the collected data is either barely sufficient for statistical evaluation or there is the possibility that the investigated area does not represent the overall sample structure.

Another method to determine the size and shape of nanostructures is small-angle X-ray scattering (SAXS), which is a well-established technique for the investigation of structure sizes in the nanometer and micrometer regimes [13]. SAXS is widely used but so far not often for deposited clusters and clusters embedded in matrices. For non-biological samples the radiation damage that X-rays can inflict is negligible and therefore we can probe the sample non-destructively. SAXS is a method that provides information on the ensemble average of particle sizes and shapes. The exact and simultaneous determination of the shape and size distributions of the scattering entities is in general not possible. In order to be able to interpret the data, approximations concerning the particle shape and size distributions are necessary. One has to make assumptions of the particle shape (e.g. spherical) and/or of size distribution (e.g. Gaussian). Despite these limitations, SAXS is a technique which, in combination with complementary techniques, can provide useful information on the sample structure. For instance, SAXS was used to determine the size of gold nanoparticles in solution [14] and silver clusters in a glass matrix [15]. Also, platinum clusters in different matrices were subject of several SAXS investigations [16–18]. Insights into the size and growth process of chromium-containing nanoparticles grown from a glassy matrix can be quoted as another example [19].

Here we present a comprehensive study of clusters with a well-defined size distribution in the gas phase which were co-deposited with a matrix onto a substrate. As investigation tools SAXS, TEM, and time-of-flight mass spectrometry were used. This enables a direct comparison between the results determined by SAXS and those of TEM and mass spectrometry.

✉ Fax: +32-16-327983, E-mail: peter.lievens@fys.kuleuven.be

Also, we studied the influence of the substrate temperature during the sample production on the final size of the cluster ensembles. We investigated gold and erbium clusters because of their particular optical properties [6, 20] and iron–platinum and cobalt clusters because they are of interest in the field of magnetism [21–24].

2 Experimental data and results

2.1 Cluster production and co-deposition

For cluster production a laser vaporization source was used, which is described in detail elsewhere [21, 25, 26], so that we will suffice here with only a brief description. The required cluster material is vaporized by focusing nanosecond laser pulses from a frequency-doubled Nd:YAG laser ($\lambda = 532$ nm, $\tau = 7$ ns, repetition rate 10 Hz) on a target of the desired cluster material. The volume above the target is synchronously flushed by a pulse of helium gas, which cools the ablated material. The supersaturated ablation plume expands through a nozzle with a conical aperture into vacuum (base pressure $p = 10^{-8}$ mbar), which stops the cluster growth. The cluster formation is mainly controlled by the time delay between the He gas pulse and the laser pulse, but also by the laser power, the nozzle diameter, and the formation chamber volume. These are important parameters which differ for each cluster material [25]. The cluster beam passes a skimmer and reaches the deposition chamber (base pressure $p = 10^{-9}$ mbar) after being led through a differentially pumped vacuum section. The clusters were deposited with low kinetic energy (< 0.5 eV/atom) on the substrate [26]. The cross section of the cluster beam on the sample surface is circular with a diameter of about 13 mm. By using Rutherford backscattering spectroscopy we verified that the amount of deposited material from the cluster beam is constant over the 5×10 mm²-sized samples.

Freshly cleaved mica with a thickness of about 20 μ m was used as substrate. After annealing the substrates for 30 min at 500 °C under ultra-high-vacuum conditions, a 20-nm-thick buffer layer of magnesium oxide (MgO) was evaporated from a Knudsen cell whilst the substrate temperature was kept at 500 °C. With atomic force microscopy we observed that under these conditions a closed MgO layer is grown. When using lower substrate temperatures, large flat MgO islands with diameters of about 100 nm are generated, a result which is in agreement with the literature [27]. These MgO islands on the surface of the MgO layer are large compared to the cluster size and thus one can assume that all clusters are surrounded locally by the matrix material during co-deposition.

After deposition of the buffer layer, the samples were either kept at 500 °C or cooled to 140 °C. The latter temperature is determined by the heat radiation from the Knudsen cell. The clusters were co-deposited simultaneously with MgO and are, consequently, embedded in the matrix. The amount of deposited material was measured with a quartz-crystal microbalance. For MgO, growth rates of approximately 0.15 Å/s were used and the clusters were deposited with typical rates of about 300 clusters/ μ m² s. This corresponds to an atomic layer deposition rate of 4 monolayers/min for MgO and of approximately 0.5 monolayers/min for the clusters. From these values we estimate that the thickness of

the composite film was in all samples approximately 110 nm and the average cluster-center separation was at least 4.5 nm. Finally, a top layer of 20-nm MgO was deposited in order to prevent cluster oxidation.

2.2 Mass spectrometry

For mass spectrometry (MS) investigations, retractable extraction grids were inserted in the beam to accelerate the ionized clusters and to separate the different masses. The clusters were detected in the deposition chamber by a dual microchannel plate detector following electrostatic reflection. The mass resolution of the reflectron time-of-flight mass spectrometer typically is $M/\Delta M = 1000$ [26]. Since only ionized clusters are detected, while neutral clusters are also used for deposition, it was necessary to verify that the mass distributions of these clusters are representative for the neutral clusters. For this purpose the neutral clusters were ionized in front of the extraction grids by laser light from an ArF excimer laser ($\lambda = 193$ nm) and the mass distributions were compared to those of non-ionized clusters. Besides the increased integral intensity, significant differences of neither the widths nor the center positions of the mass distributions were found.

The mass-distribution spectra of the metal clusters were recorded before and after sample preparation. A representative data set of each cluster material is depicted in Fig. 1. The cluster radii were calculated from the cluster masses by using the specific density and the molar volume of the corresponding bulk material. For small radii, single clusters can be resolved but for larger sizes overlap between the single-cluster peaks in the mass-distribution spectrum occurs and a broad ‘hump’ is observed. Only in the case of Au and Er clusters were some of the smaller clusters composed of less than 10 atoms produced and detected. For Au clusters the corresponding part of the spectrum with radii between 1.8 Å and 4.8 Å was cut out because the detector was saturated. These small clusters play hardly a role for TEM and SAXS as the in-

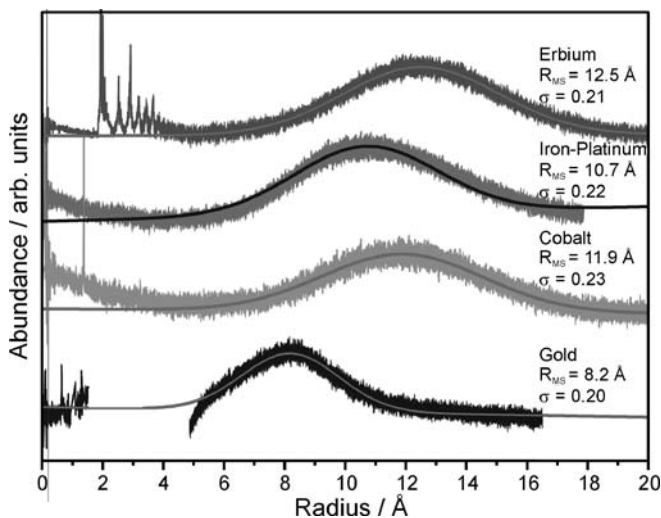


FIGURE 1 Radius distributions of metal clusters before co-deposition determined from mass spectrometry. The solid lines represent Gaussian curves used to extract the particle radii given in the figure. In the case of Au clusters the data between 1.8 Å and 4.8 Å was distorted and therefore removed (for details see text)

tegrated amount of material contributed by these very small clusters is low compared to that in the larger particles [21].

For all spectra Gaussian functions were fitted to the peaks of the larger clusters (Fig. 1, solid lines) and the mean radii were extracted. The cluster radii and the relative widths σ (half width at half maximum divided by cluster radius) of the distributions are included in Fig. 1. As the cluster production is crucially dependent on several parameters, e.g. the temperature of the cluster source, we observed some changes of the mean cluster radii during the two hours of sample production, which can be attributed to some time-dependent fluctuations of the control parameters. These variations of the mean radii by about 0.5 to 1 Å were accounted for in the error bar estimates. The averaged values from the mass spectra before and after cluster film production are compiled in Table 1. The smallest produced nanoclusters were the Au clusters with $R_{MS} = 8$ Å and the largest were the Er clusters with an average radius of about $R_{MS} = 12.6$ Å. The relative widths of the distributions were in all cases estimated to be $\delta = 0.22 \pm 0.03$.

2.3 Transmission electron microscopy

The only difference in sample preparation for the TEM measurements, compared to the procedure outlined in Sect. 2.1, was that small NaCl crystals were used as substrate. A schematic cross section of a sample is depicted in the inset of Fig. 2a. The MgO matrix containing the embedded clusters was separated from the substrate by dissolving the NaCl in distilled water. The free-standing cluster matrix film was then caught on a carbon-coated TEM grid. The samples were dried and directly investigated with high-resolution TEM using a Jeol 4000EX HREM microscope operating at an acceleration voltage of 400 kV with a point-to-point resolution of 0.17 nm.

Two samples, one containing Co clusters, the other containing FePt clusters, in MgO matrices that were prepared at a substrate temperature of 140 °C were analyzed. An in-plane TEM micrograph of the sample containing FePt clusters is shown in Fig. 2a. Single clusters are clearly resolved and the assumption that they are predominantly spherical is confirmed. In the lower right part of Fig. 2a, where the thickness of the prepared part of the layer is the thinnest, it can be seen that the clusters are also well separated. The radius distribu-

Material	$T/^\circ\text{C}$	$R_{MS}/\text{Å}$	$R_{TEM}/\text{Å}$	$R_{SAXS}/\text{Å}$
Au	140	9 ± 1		$9.4 \pm 0.2^*$
FePt	140	10.6 ± 0.1	10.4	$10 \pm 0.2^*$
Co	140	12.2 ± 0.5		$10.4 \pm 0.2^*$
Er	140	12.6 ± 0.5		$11.2 \pm 0.2^*$
Au	500	8 ± 1		11.9 ± 0.2 11.8 ± 1.1 12.4 ± 0.5 $14.6 \pm 1.6^*$
Co	500	11.7 ± 0.5		$14.1 \pm 0.5^*$ 16.2 ± 0.9

TABLE 1 Comparison of the experimental data in dependence on material and temperature during preparation. The radii extracted by mass spectrometry (MS) are average values from data recorded before and after preparation. The error bar of the SAXS data represents the quality of the linear fit. The values marked with an asterisk correspond to the data plotted in Fig. 3

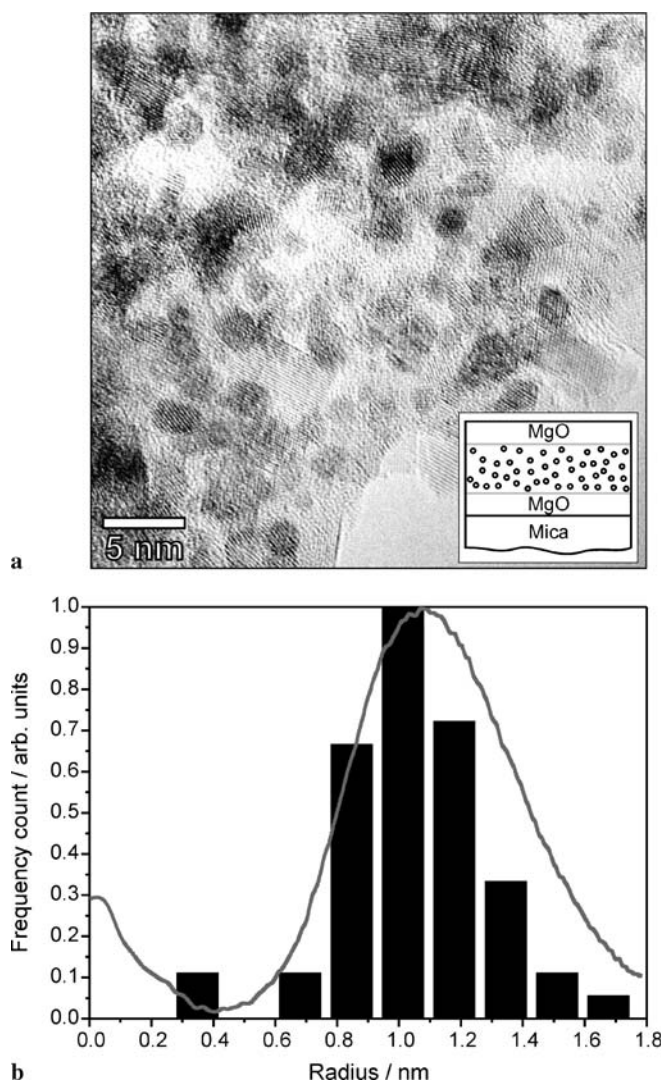


FIGURE 2 (a) Transmission electron micrograph of FePt clusters embedded in an MgO matrix. *Inset:* schematic cross section of the investigated samples (not drawn to scale), (b) statistical evaluation of the micrograph (black bars) in comparison with the radius distribution from mass spectrometry (solid line)

tion extracted from the TEM data is plotted in Fig. 2b (black bars). The size distribution of the FePt clusters is in good agreement with the results from mass spectrometry (solid line). An average radius of $R_{TEM} = 10.4$ Å and a relative size distribution width of $\sigma = 0.23$ are obtained from this data. For Co clusters in MgO, only a qualitative evaluation was possible, as the TEM micrograph did not sharply resolve single clusters due to a larger substrate thickness (figure not shown). However, in that case no structures larger than about 40 Å were visible.

2.4 Small-angle X-ray scattering

The small-angle X-ray scattering experiments have been carried out at the Dutch–Belgian beamline ‘DUBBLE’ at the European synchrotron radiation facility (ESRF) in Grenoble [28]. The sample was oriented perpendicular to the incident X-ray beam ($\lambda = 1.42$ Å, $E = 10$ keV, beam size 0.15 mm \times 0.23 mm, 16-bunch mode) with the matrix layer

facing the X-ray beam. The samples were mounted on an x - y scanning table which allowed us to perform SAXS measurements at different positions of the sample surface. One quadrant of the isotropic scattering pattern was detected by a two-dimensional multiwire gas-filled detector at a distance of 2.8 m behind the sample [29]. The scattering vector scale was calibrated using a silver behenate diffraction pattern [30]. The scattered signals were acquired for typically 60 min and radially integrated, so that a one-dimensional data set in the scattering vector range $q = 0.02$ – 0.42 \AA^{-1} ($2\theta = 0.26$ – 5.48°) was obtained. From each data set the signal from the corresponding reference sample consisting of mica with a MgO layer of equivalent thickness produced under identical experimental conditions was subtracted. Also, the signal was corrected for the detector sensitivity function.

The scattering curve of spherical objects with sufficient interdistance is given by

$$I(q) = I(0) |F(q)|^2 S(q), \quad (1)$$

where $S(q)$ is the structure factor, describing the spatial distribution of the clusters, and $F(q)$ is the so-called form factor. For widely separated particles we can assume that $S(q) = 1$. In the low-angle regime the form factor can be approximated by the Guinier approximation. The scattering function results in [13]

$$I(q) \propto (\Delta n_e)^2 e^{-q^2 R_g^2/3}. \quad (2)$$

The amplitude of the scattering is determined by the difference of the electronic densities Δn_e of the participating materials and a decreasing exponential function. In the exponent, R_g is the radius of gyration, which is, for spherical particles, related to the real particle radius by $R_g^2 = 3/5 (R_{\text{SAXS}})^2$ [13]. From (2) it can be seen that the radius of gyration can be derived by plotting the data in a $\ln(I(q))$ versus q^2 plot. In the appropriate q -range, the slope of the linear part can be used to calculate R_g .

For particle ensembles with a size dispersion, a further correction is necessary because the scattering cross section is proportional to the cluster volume and therefore larger particles are overestimated in the Guinier plots. We found by simulation that the maximum of a volume-weighted Gaussian size distribution $r^3 f_G(r)$ with $\sigma_R = 0.22$ is shifted to larger radii by a factor of 1.13 compared to the usual Gaussian radius distribution $f_G(r)$. Therefore, the radii determined by SAXS were divided by this correction factor in order to represent the average radius of the particle ensembles.

The scattering curves for the embedded clusters prepared at different temperatures are shown in Fig. 3. In the range of approximately $q^2 = 0.03$ – 0.10 \AA^{-2} a linear decrease of the scattering intensity is observed for all cluster materials. This is the region which is associated with structure sizes of $d = 2\pi/q = 31$ – 20 \AA , i.e. with the typical dimensions of the clusters. The linear fits in the range $q^2 = 0.03$ – 0.10 \AA^{-2} are indicated by the straight solid lines in Fig. 3. Using the formalism outlined above, R_{SAXS} is deduced from the obtained fitting parameters (see Table 1). The data obtained from Fig. 3 are marked with an asterisk in the table. The scattering curves of samples prepared at 500°C have a stronger fall-off because for larger clusters the X-rays are preferably scattered

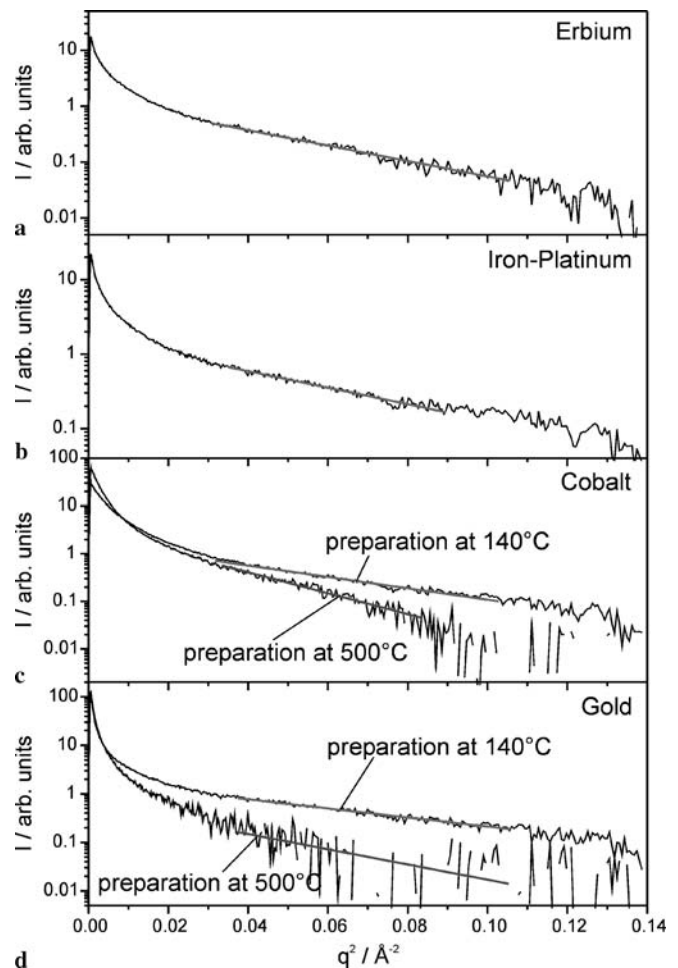


FIGURE 3 Small-angle scattering patterns from samples containing (a) erbium, (b) iron–platinum, (c) cobalt, and (d) gold clusters. The straight solid lines represent linear fits employing (1). The data have been obtained from samples prepared at 140°C [(a)–(d)] and additionally from samples prepared at 500°C [(c), (d)]

into a smaller q -range. Thus, for large q -values the signal is noisier compared to that of samples produced at 140°C . The values in Table 1 are determined from different positions of the sample. The slight variations of the average radii beyond the error bars are due to, as yet undetermined, systematic influences during sample preparation.

However, the influence of the preparation temperature on the slope of the SAXS data, i.e. the cluster radius, is obvious (Fig. 3c and d). For example, the radius for Co clusters prepared at 500°C is $R_{\text{SAXS}} = 14.1 \pm 0.5 \text{ \AA}$ and thus is significantly larger than $R_{\text{SAXS}} = 10.4 \pm 0.2 \text{ \AA}$ that was extracted from the data of the sample prepared at 140°C .

3 Discussion

For the cluster samples prepared at a temperature of 140°C the radii extracted from the TEM micrographs are in excellent agreement with the data from mass spectrometry for the FePt clusters (Table 1). Also, in the case of Co clusters the agreement is reasonable (see Sect. 2.3). This fact, and the absence of partially coalesced clusters in the TEM images, indicates that the size and shape of the clusters are conserved after embedding them in the matrix. As expected for low en-

ergy cluster beam deposition [3], the clusters neither fragment nor penetrate the substrate surface upon impact. Thus, it is confirmed that no fragmentation, coalescence, or diffusion has occurred during the co-deposition of these clusters at this temperature of 140 °C. In conclusion, nanoclusters embedded in a matrix can serve as a well-defined basis to benchmark the capability of the SAXS measurements for this type of sample.

Next, we compare the average particle radii derived from the SAXS experiment with those from mass spectrometry. This direct comparison is possible for the samples prepared at 140 °C, since the TEM results proved that the size of the nanoparticles was not changed during embedding them in the MgO matrix.

Guinier radii were successfully obtained from the SAXS data for all investigated samples. A typical statistical fitting error of only 0.2 Å was found for all data sets. This value turned out to be lower than the reproducibility of the measurements at different sample positions. For erbium cluster films where measurements were performed at two different positions on the sample, average sizes differing by about 0.7 Å were found. Assuming this value to be the typical systematic error, the radii extracted by SAXS agree well with the data from mass spectrometry. The relationship between the radii determined by the different techniques, i.e. by SAXS and mass spectrometry, is depicted in Fig. 4 by filled squares. A linear function, which was forced to go through the origin of the graph, was used to fit the data of these samples, which were prepared at 140 °C. A ratio of $R_{\text{SAXS}}/R_{\text{MS}} = 0.92 \pm 0.03$ was found. Under ideal circumstances, meaning that the data were perfectly in agreement, a value of 1 should have been obtained (i.e. $R_{\text{SAXS}} = R_{\text{MS}}$). The deviation of this value from 1 is possibly caused by the fact that the approximations made for the Guinier analysis or the size polydispersity are not fulfilled; for instance, the assumptions that the scattering entities would be spherical or the usage of a Gaussian particle size distribution. Nevertheless, this correlation between the radii determined by the two methods shows the capability of small-angle X-ray scattering to determine an average particle radius which is in reasonable agreement with other experimental techniques which are more traditionally used in this field.

The findings of our study are in good agreement with other studies where TEM results were also compared to the radii from SAXS measurements [14, 31]. Gold clusters with radii of 11–22 Å dispersed in a solution synthesized from HAuCl_4 were studied in that case [14]. The cluster solution was directly used for the SAXS measurements and was drop-cast on carbon-coated grids for TEM studies. The values extracted from the Guinier analysis were about 10% larger than the results from the TEM investigations. This effect was attributed to the overestimation of the large clusters in the Guinier plots [14]. Ramallo-Lopez et al. [31] studied platinum clusters that were prepared by incipient wetness impregnation of porous Al_2O_3 , ZrO_2 , and $\text{ZrO}_2\text{-CeO}_2$ with aqueous $\text{H}_2\text{PtCl}_6 \cdot 6\text{H}_2\text{O}$ solutions and subsequent reduction with H_2 . In that case for TEM the samples were crushed, suspended in isopropanol, and superimposed on a carbon-coated copper grid. With SAXS only small clusters with radii of 6–7 Å were detected, whereas with TEM larger clusters with radii of 28–49 Å were also found in the samples [31]. In both publications an agreement between the radii extracted from SAXS

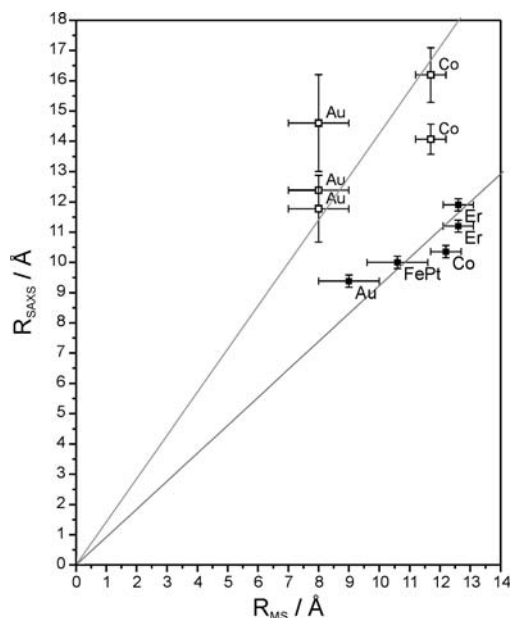


FIGURE 4 Comparison of the cluster radii before (*horizontal axis*) and after (*vertical axis*) embedding the clusters in the MgO matrix. The samples have been prepared at 140 °C (*filled squares*) and 500 °C (*open squares*). The *solid lines* are linear fits through the origin. Slopes of $R_{\text{SAXS}}/R_{\text{MS}}$ (140 °C) = 0.92 ± 0.03 and $R_{\text{SAXS}}/R_{\text{MS}}$ (500 °C) = 1.43 ± 0.10 have been extracted

and TEM was found. However, in our measurements we were able to investigate a well-defined system of embedded clusters by TEM and mass spectrometry without making major changes in the sample preparation. In particular, we could successfully determine the dimensions of the metal clusters with transmission X-ray scattering despite the relatively thick mica substrate and the surrounding MgO matrix.

Our results confirm the reliability of SAXS measurements as far as average size measurement is concerned. Using this fundamental finding we have investigated the influence of the substrate temperature during cluster co-deposition, i.e. during embedding the clusters in the MgO matrix. In addition to the data of the particles embedded in the MgO matrix at 140 °C discussed before (Fig. 4, filled squares), the data of the particles co-deposited at a temperature of 500 °C are included in Fig. 4 (open squares). The radii of the clusters in the matrix are significantly larger, which should be attributed to heat-induced effects, such as cluster diffusion and coalescence that are thermally activated processes and appear preferably at higher substrate temperatures [3]. In our case the rapid cluster diffusion is stopped as soon as enough matrix material is deposited and the clusters are immobilized. After embedding the particles in the matrix, diffusion of atoms from smaller clusters to the larger ones, i.e. Ostwald ripening, is expected at elevated temperatures [32–34]. In both processes the number density of the particles decreases while the remaining particles are growing.

Admittedly, other effects such as oxidation or formation of alloys with the matrix material could cause an increase of the nanoparticle radii and changes of particle compositions at elevated temperatures. Since the gold clusters which are chemically inert also exhibit an increase in size at 500 °C, these effects are unlikely to cause the observed increased cluster size.

In order to estimate the relationship between the cluster radii before and after embedding, a linear function was used to fit the data for the samples prepared at 500 °C. A slope of $R_{\text{SAXS}}/R_{\text{MS}}(500\text{ °C}) = 1.43 \pm 0.10$ was obtained. Compared to the slope of $R_{\text{SAXS}}/R_{\text{MS}}(140\text{ °C}) = 0.92 \pm 0.03$ for the clusters grown at 140 °C, at 500 °C the clusters tend to have an approximately 50% increase in their average radius. We attribute this to temperature-induced coalescence and Ostwald ripening during the sample preparation as discussed before.

An increase of the cluster radius upon annealing was also observed by Müller et al. who investigated large platinum clusters embedded in an alumina matrix with SAXS [16]. An increase of the average particle radius from 70 to 106 Å was observed. The difference with our experiments is that the cluster film was tempered after preparation at 800 °C for 100 h and the sample was at room temperature during preparation.

Also, films consisting of Fe₃Pt and FePt clusters with radii of 22.5 ± 5 Å have been investigated [21]. These cluster layers were annealed after preparation at different temperatures for one hour and investigated with TEM, X-ray diffraction, and magnetization measurements. Besides a transition from face-centered-cubic to face-centered-tetragonal phase inside the FePt clusters, at temperatures above 550 °C strong coalescence was observed. Despite the missing MgO matrix, these results agree with our findings concerning the occurrence of larger clusters at the elevated preparation temperatures.

4 Conclusions

In a comparative study we have measured the size of embedded clusters, created by laser vaporization and cluster beam deposition, with mass spectrometry, TEM, and SAXS. By using TEM we verified that the clusters retained their size after embedding in the matrix at a temperature of 140 °C. The comparison between these results with the data from small-angle X-ray scattering showed a good agreement between the cluster radii for the samples which were prepared at 140 °C as determined by the different methods. Thus, we conclude that transmission SAXS can be an adequate method to determine the dimensions of nanoparticles in a matrix even when the nanoparticle/matrix composite is deposited onto a relatively thick substrate.

Furthermore, we used SAXS to extract the size of particles which were embedded at 500 °C in the MgO matrix. The radii of these clusters were significantly larger, by a factor of approximately 1.5. We attribute these increased dimensions to the incidence of coalescence and Ostwald ripening during the co-deposition of the clusters at elevated temperatures.

ACKNOWLEDGEMENTS This work was supported by the Fund for Scientific Research – Flanders (FWO), the Belgian Interuniversity Attraction Poles (IAP/P5/01), the Flemish Concerted Research Action (GOA/2004/02), and the European Union's Human Potential (NanoCluster HPRN-CT-2002-00328) research programs. Access to beamline BM26B of the ESRF was made possible under an NWO-FWO collaborative agreement. Florian Meneau, Jeroen Jacobs, and Dirk Detollenaere are kindly thanked for their technical support.

REFERENCES

- 1 K.H. Meiwes-Broer (ed.), *Metal Clusters at Surfaces: Structure, Quantum Properties, Physical Chemistry* (Springer Ser. Cluster Phys.) (Springer, Berlin, 2000)
- 2 C. Binns, *Surf. Sci. Rep.* **44**, 1 (2001)
- 3 A. Perez, P. Melinon, V. Dupuis, P. Jensen, B. Prevel, J. Tuaille, L. Bardotti, C. Martet, M. Treilleux, M. Broyer, M. Pellarin, J.L. Vaille, B. Palpant, J. Lermé, *J. Phys. D Appl. Phys.* **30**, 709 (1997)
- 4 U. Heiz, A. Sanchez, S. Abbet, W.D. Schneider, *J. Am. Chem. Soc.* **121**, 3214 (1999)
- 5 K. Koga, T. Ikeshoji, K. Sugawara, *Phys. Rev. Lett.* **92**, 115 507 (2004)
- 6 U. Kreibig, M. Vollmer, *Optical Properties of Metal Clusters* (Springer, Berlin, 1995)
- 7 J. Chatterjee, Y. Haik, C.J. Chen, *J. Magn. Magn. Mater.* **257**, 113 (2003)
- 8 V. Rotello (ed.), *Nanoparticles: Building Blocks for Nanotechnology (Nanostructure Science & Technology)* (Kluwer Academic/Plenum, New York, 2003)
- 9 S.A. Maier, M.L. Brongersma, P.G. Kik, S. Meltzer, A.A.G. Requicha, H.A. Atwater, *Adv. Mater.* **13**, 1501 (2001)
- 10 G.I. Frolov, *Technol. Phys.* **46**, 1537 (2001)
- 11 K.C. Grabar, K.R. Brown, C.D. Keating, S.J. Stranick, *Anal. Chem.* **69**, 471 (1997)
- 12 M. Sugiyama, G. Sigesato, *J. Electron Microsc.* **53**, 527 (2004)
- 13 O. Glatter, O. Kratky, *Small Angle X-ray Scattering* (Academic, London, 1982)
- 14 M.J. Hostetler, J.E. Wingate, C.J. Zhong, J.E. Harris, R.W. Vachet, M.R. Clark, J.D. Londono, S.J. Green, J.J. Stokes, G.D. Wignall, G.L. Glish, M.D. Porter, N.D. Evans, R.W. Murray, *Langmuir* **14**, 17 (1998)
- 15 G. Kellermann, A.F. Craievich, *Phys. Rev. B* **70**, 054 106 (2004)
- 16 J. Müller, P. Löhman, D.C. Meyer, *Cryst. Res. Technol.* **40**, 177 (2005)
- 17 C.S. Tsao, C.Y. Chen, *Physica B* **353**, 217 (2004)
- 18 R.E. Winans, S. Vajda, B. Lee, S.J. Riley, S. Seifert, G.Y. Tikhonov, N.A. Tomczyk, *J. Phys. Chem. B* **108**, 18 105 (2004)
- 19 W. Bras, G.N. Greaves, M. Oversluizen, S.M. Clark, G. Eeckhaut, *J. Non-Cryst. Solids* **351**, 2178 (2005)
- 20 J.V. Pinto, R.C. da Silva, E. Alves, M.J. Soares, T. Monteiro, R. González, *Nucl. Instrum. Methods B* **218**, 128 (2004)
- 21 A.N. Dobrynin, D.N. Ievlev, G. Verschoren, J. Swerts, M.J. Van Bael, K. Temst, P. Lievens, E. Piscopiello, G. Van Tendeloo, S.Q. Zhou, A. Vantomme, *Phys. Rev. B* **73**, 104421 (2006)
- 22 S. Momose, H. Kodama, T. Uzunaki, A. Tanaka, *Appl. Phys. Lett.* **85**, 1748 (2004)
- 23 S.R. Shinde, S.B. Ogale, J.S. Higgins, H. Zheng, A.J. Millis, V.N. Kulkarni, R. Ramesh, R.L. Greene, T. Venkatesan, *Phys. Rev. Lett.* **92**, 166 601 (2004)
- 24 S. Yamamuro, K. Sumiyama, T. Kamiyama, K.J. Suzuki, *J. Appl. Phys.* **86**, 5726 (1999)
- 25 W. Bouwen, P. Thoen, F. Vanhoutte, S. Bouckaert, F. Despa, H. Weidele, R.E. Silverans, P. Lievens, *Rev. Sci. Instrum.* **71**, 54 (2000)
- 26 N. Vandamme, E. Janssens, F. Vanhoutte, P. Lievens, C. Van Hasendonck, *J. Phys.: Condens. Matter* **15**, S2983 (2003)
- 27 R.J. Kennedy, P.A. Stampe, *J. Magn. Magn. Mater.* **195**, 284 (1999)
- 28 W. Bras, I.P. Dolbnya, D. Detollenaere, R. van Tol, M. Malfois, G.N. Greaves, A.J. Ryan, E. Heeley, *J. Appl. Cryst.* **36**, 791 (2003)
- 29 A. Gebriel, *Nucl. Instrum. Methods* **201**, 232 (1982)
- 30 T.C. Huang, H. Toraya, T.N. Blanton, Y. Wu, *J. Appl. Cryst.* **26**, 180 (1993)
- 31 J.M. Ramallo-Lopez, F.G. Requejo, A.F. Craievich, J. Wei, M. Avalos-Borja, E. Iglesia, *J. Mol. Catal. A Chem.* **228**, 299 (2005)
- 32 G. Rosenfeld, K. Morgenstern, M. Esser, G. Comsa, *Appl. Phys. A* **69**, 489 (1999)
- 33 M.J.J. Jak, C. Konstapel, A. van Kreuningen, J. Verhoeven, J.W.M. Frenken, *Surf. Sci.* **457**, 295 (2000)
- 34 C.E.J. Mitchell, A. Howard, M. Carney, R.G. Egdell, *Surf. Sci.* **490**, 196 (2001)